

Programming Heterofunctional Active Sites via *In Situ* Reticular Editing of Metal–Macrocyclic Frameworks

Junyu Ren,[#] Yanpei Song,[#] Yingxiang Ye, Peter VanNatta, Yin Zhang, Abdullah M. Al-Enizi, Ayman Nafady, Kui Tan, and Shengqian Ma*



Cite This: *J. Am. Chem. Soc.* 2026, 148, 17218–17227



Read Online

ACCESS |



Metrics & More

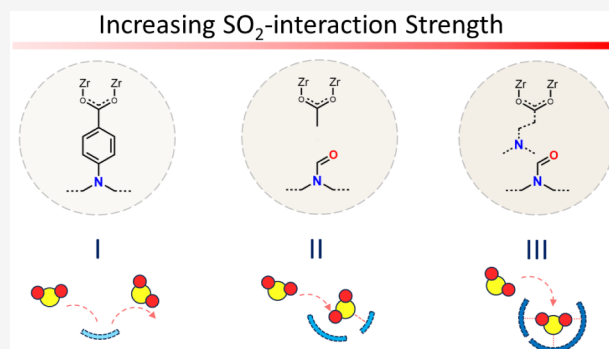


Article Recommendations



Supporting Information

ABSTRACT: In metal–organic frameworks, the scaffold serves as a passive host matrix, relying primarily on the assembly of prefunctionalized ligands to define the pore environment. Constructing cooperative binding pockets via this approach is often impeded by synthetic complexity and the steric hindrance of bulky functional groups. Herein, we present the design of two robust, tertiary amine-embedded cyclen-based ligands: one tetratopic and the other T-shaped tritopic. The two ligands were used to synthesize three isostructural, highly porous Zr-metal–macrocyclic frameworks (MMCFs), denoted as MMCF-5, MMCF-7-AcOH, and MMCF-7-AA. We highlight that the tritopic ligand enabled the framework as a reactive matrix through a strategy termed *in situ* reticular editing (ISRE). Utilizing SO₂ as a probe to interrogate the pore environment, MMCF-7-AA exhibits an exceptional capacity of 12.5 mmol g⁻¹ at 1 bar and 1.43 mmol g⁻¹ at 2500 ppm. These metrics not only position it among the top-performing adsorbents at low partial pressures but, more importantly, corroborate the successful construction of the cooperative binding sites. We then elucidated this distinct SO₂ sorption behavior through X-ray crystallography, density functional theory (DFT) calculations, and *in situ* diffuse reflectance infrared Fourier transform (DRIFT) spectroscopy. This work establishes ISRE as a versatile blueprint for pore editing, offering a feasible pathway to evolve sophisticated chemical environments by harnessing simple precursor scaffolds as reactive matrices.



INTRODUCTION

Metal–organic frameworks (MOFs) utilize metal ions and organic ligands to construct customizable porous architectures, demonstrating potential in a myriad of fields such as catalysis, sensing, and gas storage/separation.^{1–3} However, constructing sophisticated, cooperative microenvironments within these scaffolds remains synthetically elusive. Existing methodologies are fundamentally limited by the trade-off between complexity and structural integrity. The prefunctionalization strategy, while allowing precise ligand design, often suffers from steric congestion exerted by bulky functional groups during assembly, which leads to amorphous precipitates, structural defects, or the formation of undesired topological phases.^{4,5} On the other hand, postsynthetic modification (PSM) attempts to circumvent assembly issues but inevitably compromises the structural integrity and faces significant diffusion limitations. The restricted transport of reagents into the confined pores often results in chemical inhomogeneity, creating a functionalization gradient between the exterior surface and the interior core.^{6,7} Under these conditions, one may imagine that an ideal synthetic paradigm would allow the framework to evolve complexity *in situ* from sterically minimal precursors. Such a strategy would leverage the scaffold as a

reactive matrix to construct sophisticated microenvironments without compromising structural integrity or homogeneity.

Polyaza-macrocycles, distinguished by their rigid cyclic geometries and rich chemistry, serve as versatile scaffolds for constructing tertiary-amine-based ligands.⁸ Prominent examples of this class include 1,4,7-triazacyclononane (TACN), 1,4,7,10-tetraazacyclododecane (cyclen), and 1,4,8,11-tetraazacyclotetradecane (cyclam).^{9–11} These macrocycles have been widely reported as building blocks for engineering MOFs applied in catalysis, molecular/ion recognition, and gas separation.¹² The inherent secondary amine sites within these macrocycles function as potent nucleophiles, which can be activated through diverse pathways, such as N-alkylation, N-arylation, and N-acylation.^{13–15} This reactivity allows for the precise installation of coordinating arms or functional pendants, enabling the fine-tuning of the microenvironments.

Received: January 31, 2026

Revised: April 2, 2026

Accepted: April 8, 2026

Published: April 16, 2026



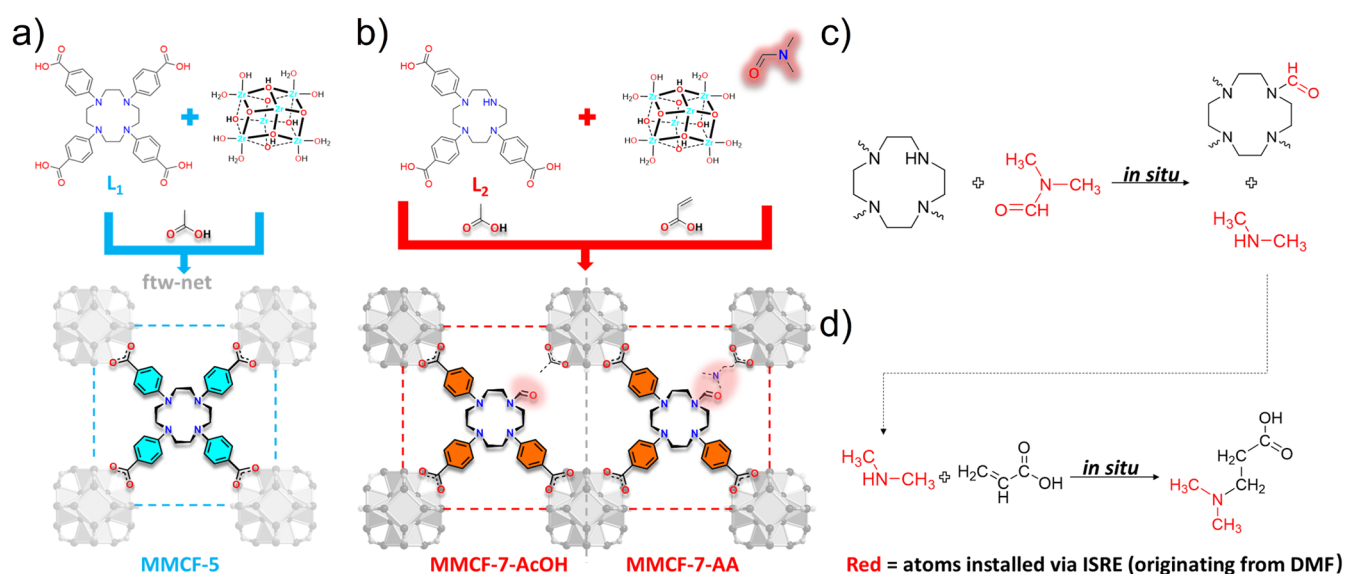


Figure 1. Assembly of Zr-MMCFs from cyclen-based linkers and the *in situ* reticular editing (ISRE) chemistry. (a) The tetrapotic ligand L_1 reacts with $ZrCl_4$ in DMF using acetic acid as the modulator to form MMCF-5 with ftw topology. (b) The tritopic ligand L_2 , bearing one free secondary amine (N–H) on the cyclen ring, reacts with $ZrCl_4$ in DMF to form MMCF-7-AcOH (acetic acid as modulator) and MMCF-7-AA (acrylic acid as modulator). During crystallization, two concurrent *in situ* reactions take place: (c) N-Formylation—DMF acts as a formylating agent, reacting with the secondary amine of L_2 to install a formamide (N–CHO) functionality; dimethylamine is released as a byproduct. (d) Aza-Michael addition (MMCF-7-AA only)—the liberated dimethylamine undergoes conjugate addition to the acrylic acid modulator, generating 3-(dimethylamino)propionic acid, which is incorporated into the framework. Red highlights indicate atoms originating from the DMF.

While *N,N*-dimethylformamide (DMF) is predominantly utilized as a polar aprotic solvent in MOF synthesis, its role can extend beyond that of a reaction medium. Importantly, DMF is a well-established N-formylating agent: under solvothermal conditions, it can react directly with nucleophilic secondary amines to yield formamide (N–CHO) functionalities, releasing dimethylamine as a byproduct.^{16,17} This reactivity is mechanistically distinct from DMF hydrolysis, which produces formic acid and free dimethylamine; in the N-formylation pathway, the carbonyl carbon of DMF is transferred intact to the amine nitrogen, generating a tertiary amide rather than a free aldehyde.¹⁸ Although such DMF-mediated transformations are frequently observed as uncontrolled side reactions during MOF synthesis, they represent an untapped opportunity for deliberate framework modification—provided that suitable nucleophilic handles are built into the ligand by design.

Developing regenerable adsorbents for the deep purification of downstream flue gas or tail-gas streams is critical to complement energy-intensive scrubbing technologies.¹⁹ Success in this domain hinges on the engineering of pore microenvironments, where the distinct positioning of Lewis basic sites (O/N-donors) governs the capture efficiency via weak interactions.^{20,21} However, constructing such cooperative binding motifs within stable porous scaffolds remains challenging. Conventional adsorbents, particularly those dependent on sensitive open metal sites, often lack the requisite stability or the ability to host these interacting sites with subnanometer precision, necessitating novel reticular design strategies.^{22–24}

To realize the above vision, herein we present a synthetic strategy termed *in situ* reticular editing (ISRE). Distinct from passive scaffold assembly, this strategy harnesses the intrinsic reactivity of DMF as an N-formylating agent—not as a side reaction to be suppressed, but as a tool to actively sculpt the

pore landscape. To validate ISRE for precision pore editing, we targeted constructing cooperative tertiary-amine-based microenvironments. We synthesized three macrocyclic frameworks, MMCF-5, MMCF-7-AcOH (AcOH = acetic acid), and MMCF-7-AA (AA = acrylic acid)—all crystallizing in the same cubic $Pm\bar{3}m$ framework despite differing linker geometries. In MMCF-7-AcOH and MMCF-7-AA, reactive fragments generated *in situ* are harnessed to covalently modify the developing scaffold, introducing functional complexity that is otherwise synthetically arduous. Utilizing SO_2 as a molecular probe to interrogate these evolved environments, MMCF-7-AA exhibited an exceptional uptake of 12.5 mmol g^{-1} (1 bar) and 1.43 mmol g^{-1} (2500 ppm), alongside a remarkable SO_2/CO_2 selectivity of 291 ($SO_2/CO_2 = 1/99$). The dynamic separation performance was further corroborated by column breakthrough experiments under 2500 ppm of SO_2 , highlighting a 4-fold capture enhancement for MMCF-7-AA (1.30 mmol g^{-1} at 298 K) compared to MMCF-5 (0.30 mmol g^{-1} at 298 K). The proposed transformation products were systematically confirmed via Rietveld refinement, NMR analysis, and FTIR spectroscopy. This work establishes ISRE as a pathway to evolve sophisticated chemical environments from simple precursors, offering a new dimension in reticular design beyond traditional prefunctionalization.

RESULTS AND DISCUSSION

Synthesis, Structural Characterization, and Porosity Analysis

Integrating flexible polyaza-macrocycles into rigid frameworks presents a fundamental synthetic challenge. Despite their chemical versatility, macrocycle-based porous materials often suffer from conformational disorder and structural amorphization, which obscure the Lewis basic sites and diminish their accessibility. To overcome this entropy penalty, our previous work demonstrated that rigidifying the core via direct N-

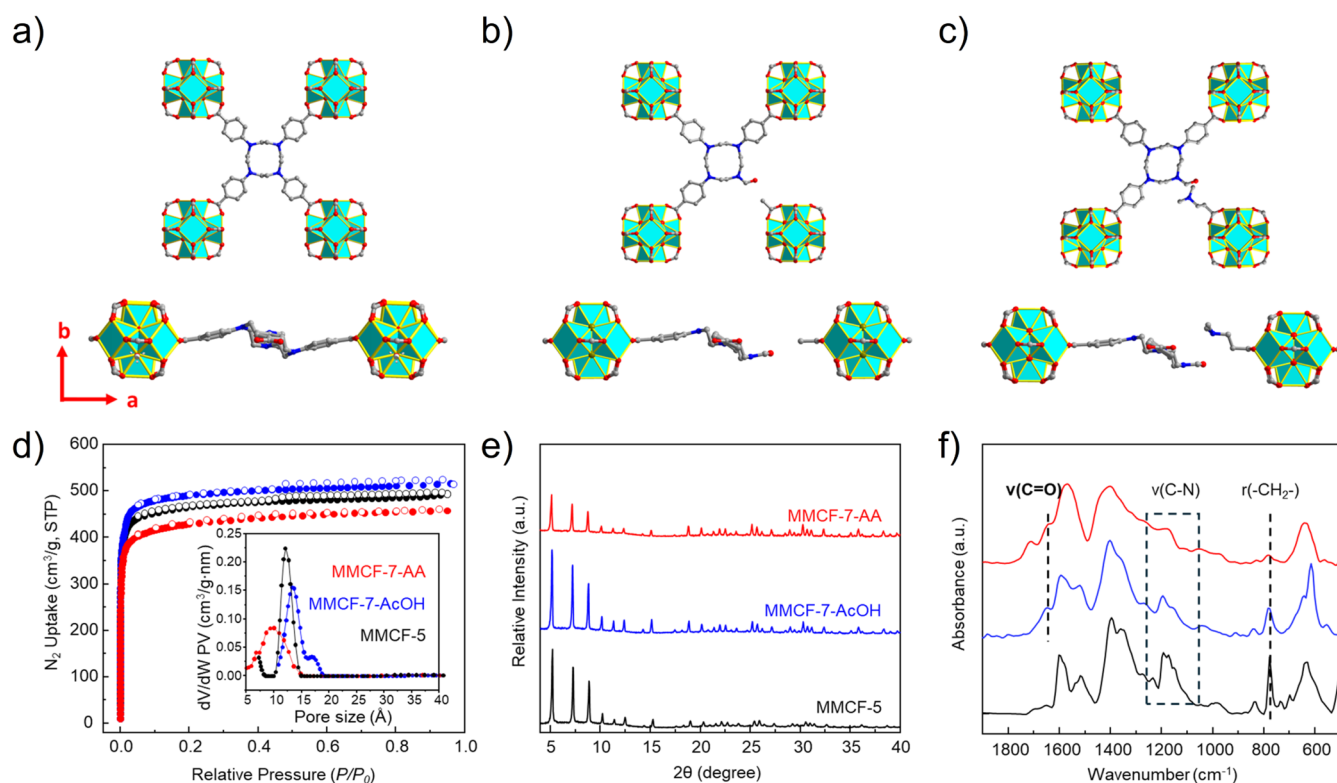


Figure 2. Structural and porosity characterization. Perspective views of the crystal structures of (a) MMCF-5, (b) MMCF-7-AcOH, and (c) MMCF-7-AA, illustrating their isostructural nature. (d) N_2 adsorption isotherms collected at 77 K (Inset: corresponding pore size distributions). (e) Experimental PXRD patterns confirming phase purity. (f) FT-IR spectra highlighting the evolution of functional groups. Assignments: ν = stretching, r = rocking. Color scheme: MMCF-5 (black), MMCF-7-AcOH (blue), and MMCF-7-AA (red).

arylation effectively suppresses intramolecular freedom, facilitating the crystallization of stable Zr-MOFs.^{14,25} Building on this strategy, we accessed the tetratopic ligand L_1 (4,4',4'',4'''-(1,4,7,10-tetraazacyclododecane-1,4,7,10-tetrayl)tetrabenzonic acid) via Buchwald–Hartwig cross-coupling (Figure S1). However, to fully harness the macrocycle as a programmable platform for ISRE, we further engineered a C_{2v} -symmetric, T-shaped tritopic ligand: 4,4',4''-(1,4,7,10-tetraazacyclododecane-1,4,7-triyl)tribenzoic acid (L_2 , Figure S2). In contrast to fully substituted L_1 , L_2 features a strategically reserved secondary amine site, establishing a latent handle for *in situ* functionalization. This molecular architecture essentially embeds a programmable chemical trigger within the structural backbone, poised to initiate the targeted reticular editing under solvothermal conditions.

MMCF-5 and MMCF-7-AcOH were synthesized via solvothermal reactions of $ZrCl_4$ with ligands L_1 and L_2 , respectively, in DMF using acetic acid as the modulator. MMCF-7-AA was synthesized by reacting $ZrCl_4$ with ligand L_2 in DMF, but with acrylic acid as the modulator (Figures 1 and S3–S10). Single crystal structure analysis reveals that MMCF-5 crystallizes in the $Pm-3m$ space group with a topology of *ftw* (Table S1), which is exemplified by MOF-525 (or PCN-221).^{26,27} The cubic structure of MMCF-5 is based on 12-connected Zr_6 -oxo clusters and the 4-connected tetratopic L_1 linker with a pore diameter of ~ 14 Å and a formula of $[Zr_6(\mu_3-O)_4(\mu_3-OH)_4(L_1)_3] \cdot (solv)_x$, $solv = \text{solvent}$ (Figure 2a and S13 and S14). Each cube is composed of six face-sharing L_1^{4-} units and eight corner-sharing $\{Zr_6O_4(OH)_4\}$ units, where each L_1^{4-} coordinates with four $\{Zr_6O_4(OH)_4\}$ units. To our delight, the phase purity demonstrated a strong tolerance for the linker

geometry. Specifically, ligand L_2 resulted in the formation of compounds isostructural to MMCF-5, crystallizing in the same cubic $Pm-3m$ space group with matching unit cell parameters (Figures 2b–c and S15–S18). During the solvothermal synthesis, the secondary amines on L_2 undergo *in situ* N-formylation by DMF, converting them to a formamide and yielding the modified linker (formyl- L_2) incorporated in the final framework. Because formyl- L_2 is tritopic rather than tetratopic, each linker occupies the crystallographic site of L_1 but contributes only 3 carboxylate connections instead of 4. With 3 linkers per Zr_6 SBU, the linker-derived connectivity is 9, and the remaining 3 coordination sites are occupied by monocarboxylate modulators, giving the per-SBU formula $[Zr_6(\mu_3-O)_4(\mu_3-OH)_4(\text{formyl-}L_2)_3(\text{modulator})_3] \cdot (solv)_x$. This is consistent with the NMR-determined linker:modulator molecular ratio of approximately 1:1 (Figures S6 and S7). The formation of formamide species was also confirmed from the Rietveld refinements and NMR results (Tables S2 and S4; Figures S3–S9). The constitutions of MMCF-7-AcOH and MMCF-7-AA were determined by 1H and ^{13}C NMR spectroscopy of acid-digested solutions of the activated samples. The results demonstrated 1:1.09 and 1:1.05 output ratios of L_2 /AcOH and L_2 /AA (Figures S6 and S7). Since the cyclen macrocycles are on the face of each cube, it maintains a relative planar conformation of cyclen, which is beneficial to provide full access to the amine sites and the possibility for further fine-tuning. Besides heterogeneous functionalization, the T-shaped ligand also enables the creation of additional structural vacancies at the Zr nodes. Through these innovative design strategies, our approach offers a tailored solution to improve SO_2 adsorption efficiency, demonstrating the

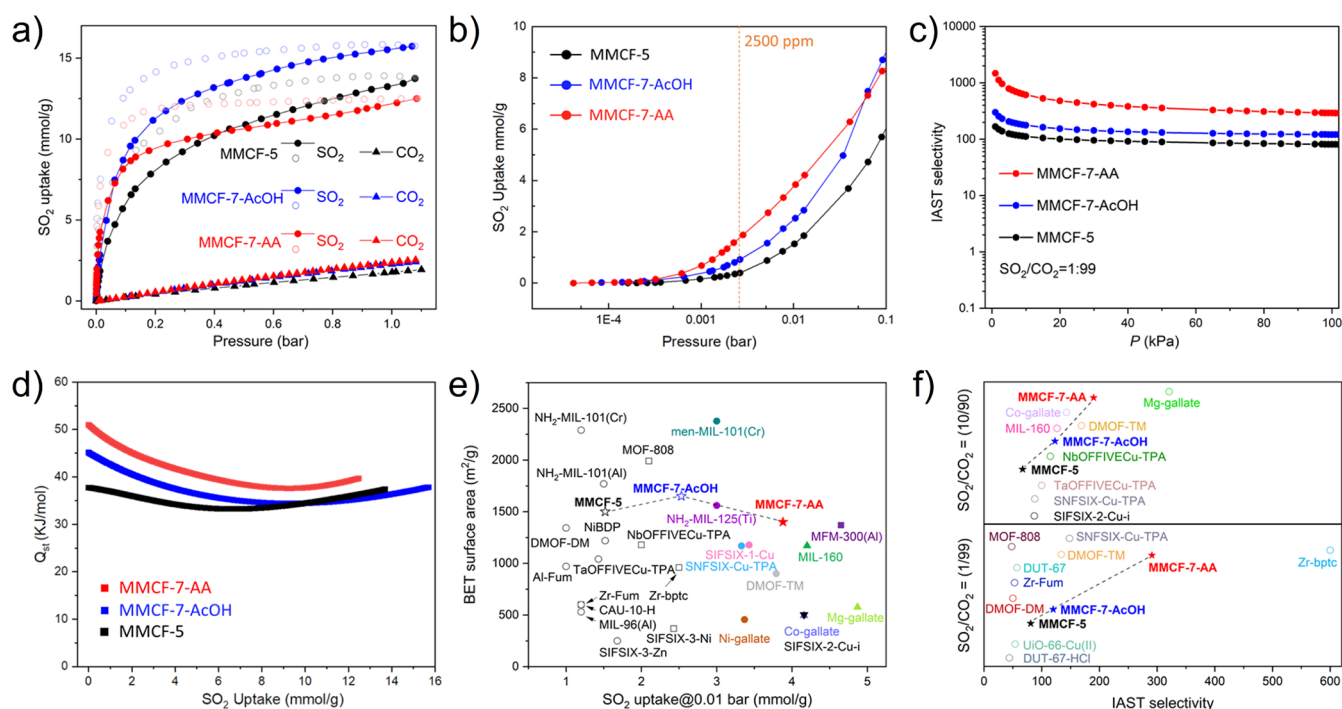


Figure 3. (a) SO_2 sorption isotherms of MMCF-5 (black), MMCF-7-AcOH (blue), and MMCF-7-AA (red) at 298 K. (b) SO_2 sorption isotherms at low partial-pressure (0–0.1 bar). (c) IAST selectivities for SO_2/CO_2 (1% SO_2 and 99% CO_2). (d) Q_{st} for uptakes of SO_2 in MMCF-5 (black), MMCF-7-AcOH (blue), and MMCF-7-AA (red). (e) Comparison of the SO_2 uptake capacities of MMCF-5, MMCF-7-AcOH, and MMCF-7-AA with state-of-the-art MOFs exhibiting uptake >1 mmol g^{-1} at 0.01 bar. A comprehensive comparison is provided in Table S6. (f) Comparison of IAST selectivities for SO_2/CO_2 at compositions of 10:90 (top) and 1:99 (bottom). A detailed comparison is summarized in Table S7.

potential of aza-macrocycle-based materials in environmental applications.

To unambiguously verify the chemical structure of the *in situ* generated $-\text{CHO}$ moieties within MMCF-7-AcOH and MMCF-7-AA, we conducted a comparative ^{13}C NMR analysis between the acid-digested MOF and an independently synthesized reference ligand, N-formyl-functionalized L_2 ($\text{L}_2\text{-CHO}$). As illustrated, the ^{13}C NMR spectrum of the digested MMCF-7-AcOH (Figure S8) and MMCF-7-AA (Figure S9) exhibits a fingerprint identical to that of the pure reference ligand (Figure S5). The most critical evidence for the successful *in situ* editing is the signal corresponding to the formyl carbonyl carbon ($\text{H}-\text{C}(=\text{O})-\text{N}$). In the reference spectrum, the formyl carbon is identified at 164.5 ppm. This exact signal is clearly resolved at a similar chemical shift range in the spectrum of the digested MMCF-7-AcOH/MMCF-7-AA, confirming the presence of the formamide moiety. This formyl peak is distinct from the carboxylic acid carbonyl signals (~ 167 ppm), ruling out misassignment. The alignment of signals in the aliphatic region (45–55 ppm, corresponding to the cyclen ring carbons) and the aromatic region (110–160 ppm) confirms that the ligand backbone remained intact during the solvothermal synthesis and that the N-formylation occurred selectively on the secondary amine site. Consequently, the identical spectral features between the digested MOF and the synthesized standard provide definitive spectroscopic proof that the MMCF-7-AcOH and MMCF-7-AA framework consists of the specific formyl-functionalized ligand generated via the *in situ* editing.

N_2 sorption isotherms were collected at 77 K to confirm the permanent porosity of MMCF-5/MMCF-7-AcOH/MMCF-7-AA after removal of the guest molecules. On the basis of the

N_2 adsorption data (Figures 2d and S22), the Brunauer–Emmett–Teller (BET) surface areas of $\sim 1500/1650/1400$ $\text{m}^2 \text{g}^{-1}$ and the total pore volume of $1.63/1.75/1.51$ $\text{cm}^3 \text{g}^{-1}$ were calculated for MMCF-5/MMCF-7-AcOH/MMCF-7-AA, respectively. It is worth noting that these are among the highest BET values reported for cyclen-based materials.^{28,29} Previously reported cyclen-based MOFs show much lower experimental BET surface areas than the theoretical value due to the inborn intramolecular freedom and thus lability involved inside the skeleton.¹² The pore size distribution calculated by nonlocal density functional theory (NLDFT) from the N_2 sorption isotherms indicates that the pores of MMCF-5, MMCF-7-AcOH, and MMCF-7-AA are predominantly distributed at 12.1, 13.3, and 10.0 Å, respectively (Figure 2d, inset). These values are systematically smaller than the crystallographic geometric pore diameter of ~ 14 Å measured from the refined models (Figures S14–S18). This discrepancy is expected: the crystallographic distance represents the atom-center-to-atom-center span across the cage, whereas the NLDFT-derived accessible pore diameter accounts for the *van der Waals* radii of the atoms.^{30,31} For MMCF-7-AA, the further reduction to 10.0 Å reflects the additional steric contribution of the *in situ* generated functional groups protruding into the pore cavity. A detailed comparison of crystallographic and sorption-derived pore dimensions is provided in Table S9.

Thermogravimetric analyses indicated that the MMCF-5 and MMCF-7-AcOH are stable up to 350 and 250 °C under a nitrogen atmosphere, respectively (Figures S23–S25). For MMCF-7-AA, the first weight loss is assigned to the residual modulator, and the framework is stable up to 250 °C (Figure S25). Even though MMCF-5/MMCF-7-AcOH/MMCF-7-AA is constructed from ligands based on flexible macrocycles, it

possesses high chemical stability in a broad variety of solvents and aqueous solutions with pH values ranging from 1 to 12 (Figures S26–S28). The PXRD patterns of MMCF-5/MMCF-7-AcOH/MMCF-7-AA remain intact after treatment at 150 °C under a nitrogen atmosphere for 24 h, indicating that crystallinity and structural integrity are retained under these thermal conditions (Figures S31–S33). It should be noted that this assessment was conducted under an inert atmosphere; long-term operational stability under simultaneous exposure to SO₂, moisture, and O₂—conditions representative of practical flue gas desulfurization—warrants further investigation. The FTIR spectra in Figure 2f show the appearance of a distinct C=O stretching band at 1657 cm⁻¹ in MMCF-7-AcOH/MMCF-7-AA, providing evidence that the secondary amine has been formylated.³² Scanning electron microscopy (SEM) was used to test the three samples' homogeneity, and it exhibited cuboctahedron crystallites measuring 5–15 μm in diameter (Figure S29). To further investigate the stability of MMCF-5/MMCF-7-AcOH/MMCF-7-AA, N₂ sorption isotherms were measured after immersing samples under water, boiling water, and pH 1 and 11 aqueous solutions for 24 h. The adsorption of N₂ by MMCF-5/MMCF-7-AcOH/MMCF-7-AA after the above treatments is comparable with that of the untreated sample, indicating the framework's resilience under harsh conditions (Figures S31–S33).

SO₂ Sorption Studies

Following the above characterizations, the SO₂ adsorption performances were evaluated for the three MOFs through static adsorption experiments. The materials demonstrated excellent SO₂ uptake at 298 K and 100 kPa (1.0 bar), with capacities reaching 13.7, 15.7, and 12.5 mmol g⁻¹ for MMCF-5, MMCF-7-AcOH, and MMCF-7-AA, respectively (Figures 3a and S42). Although this work primarily focuses on SO₂ capture under dilute conditions, MMCF-7-AcOH demonstrates a higher uptake capacity at 1 bar relative to most reported MOFs (Table S6). At 0.01 bar, the SO₂ uptake of MMCF-5 was recorded as 1.52 mmol g⁻¹, while MMCF-7-AcOH and MMCF-7-AA showed a higher uptake of 2.53 and 3.88 mmol g⁻¹, outperforming many leading MOFs such as Mg-MOF-74 (3.03 mmol/g), SIFSIX-1-Cu (3.43 mmol/g), SIFSIX-3-M variants for Ni and Zn (2.43 and 1.68 mmol/g, respectively), and NH₂-MIL-125 (Ti) (3.0 mmol/g) (Figure 3b and Table S6). As the pressure increases to 0.1 bar, the SO₂ uptake of MMCF-7-AA escalates rapidly to 8.32 mmol g⁻¹, constituting approximately 67% of its maximal capacity of 12.5 mmol g⁻¹ at 0.98 bar. This uptake exceeds that of other benchmark materials such as Zr-TPA-FA (1.8 mmol/g), NOTT-202a (2.6 mmol/g), MFM-601 (4.3 mmol/g), MFM-170 (6.2 mmol/g), DMOF-TM (6.43 mmol/g), and MFM-300 (In) (7.2 mmol/g) (Table S6). This performance conclusively demonstrates the superior SO₂ capture capability of MMCF-7-AA under lower partial pressures (<0.1 bar). To further elucidate the origin of this enhanced SO₂ affinity, we compared the BET surface areas of MMCF-5, MMCF-7-AcOH, and MMCF-7-AA against their SO₂ uptake capacities at 0.01 bar, alongside representative benchmark MOFs (Figure 3e). The benchmarking pressures of 0.01 bar were chosen to bracket the concentration range most relevant to industrial flue gas desulfurization: postcombustion flue gas typically contains 500–3,000 ppm of SO₂, while tail gases from sulfuric acid plants can reach ~1% SO₂.^{19,21} The 0.01 bar threshold also provides sufficient literature data points for a statistically

meaningful cross-material comparison, whereas direct benchmarking at 2,500 ppm is limited by the scarcity of reported values. Notably, several MOFs with higher BET surface areas deliver comparable or lower SO₂ uptake than MMCF-7-AA at these pressures, and within our isostructural series, MMCF-7-AA achieves the highest uptake despite possessing a lower BET surface area than MMCF-7-AcOH. This decoupling of textural properties from capture performance underscores the decisive contribution of the cooperative tertiary-amine-based binding pockets generated through the *in situ* reticular editing. Notably, MMCF-7-AA exhibits a SO₂ adsorption capacity of 1.43 mmol g⁻¹ at 2500 ppm, highlighting its potential as an effective sorbent under realistic flue gas conditions (Table S6). To assess the selectivity of SO₂ over CO₂, Ideal Adsorbed Solution Theory (IAST) calculations were performed on binary gas mixtures at 1 bar and 293 K. Given the trace amounts of SO₂ typically present in flue gas, high selectivity for SO₂ over other gases is crucial for a feasible adsorptive gas desulfurization process. For a molar SO₂/CO₂ ratio of 1:99, the selectivity of MMCF-5 is 81, while MMCF-7-AcOH and MMCF-7-AA achieved higher selectivities of 120 and 291, respectively (Figure 3c and Table S7). This suggests that it could play a crucial role in reducing SO₂ emissions across various industries, thereby contributing to cleaner and more sustainable energy production.

Given the highly corrosive nature of SO₂, concerns regarding the stability and regeneration of the sorbents are justified. To address these, N₂ sorption analyses (77 K) of MMCF-5, MMCF-7-AcOH, and MMCF-7-AA were conducted after 10 cycles of SO₂ sorption (Figure S30). The results confirmed that the surface areas of MMCF-5, MMCF-7-AcOH, and MMCF-7-AA remained consistent, even after 10 cycles of SO₂ exposure. In addition, the SO₂ adsorption capacity of MMCF-7-AcOH and MMCF-7-AA could be fully regenerated under mild conditions (60 °C), while MMCF-5 could be effectively recycled using a dynamic vacuum at room temperature (Figure S34).

Adsorption tests of CO₂, N₂, and CH₄ were conducted on desolvated MMCF-5/MMCF-7-AcOH/MMCF-7-AA to assess the selectivity of SO₂ over other components. At 1 bar, the CO₂ uptake capacities for MMCF-5, MMCF-7-AcOH, and MMCF-7-AA are 1.75, 2.25, and 2.51 mmol g⁻¹, respectively (Figure 3a). At 0.1 bar, the CO₂ uptake values are 0.22, 0.235, and 0.26 mmol/g for MMCF-5, MMCF-7-AcOH, and MMCF-7-AA, respectively. Compared with primary and secondary amines, tertiary amines interact with acidic compounds predominantly through electrostatic interactions, with the Lewis acidity of the sorbates playing a major role in governing the adsorption behavior. In interactions with tertiary amines, SO₂ behaves as a Lewis acid mainly through electrostatic attraction and donor–acceptor interactions involving sulfur-centered antibonding orbitals.^{33,34} This interaction, along with differences in molecular size (4.11 and 3.3 Å), dipole moment (1.63 and 0 D), and polarizability (47.7 × 10⁻²⁵ and 26.5 × 10⁻²⁵ cm³ for SO₂ and CO₂, respectively), enables tertiary amines to selectively sequester SO₂ over CO₂. For N₂ and CH₄, MMCF-5/MMCF-7-AcOH/MMCF-7-AA show negligible uptake due to the absence of strong interaction forces (Figure S50).

The affinity between the host framework and the guest molecule can be evaluated by the near-zero coverage heat of adsorption (Q_{st}). The Q_{st} values of MMCF-5, MMCF-7-AcOH, and MMCF-7-AA for SO₂ and CO₂ were obtained by

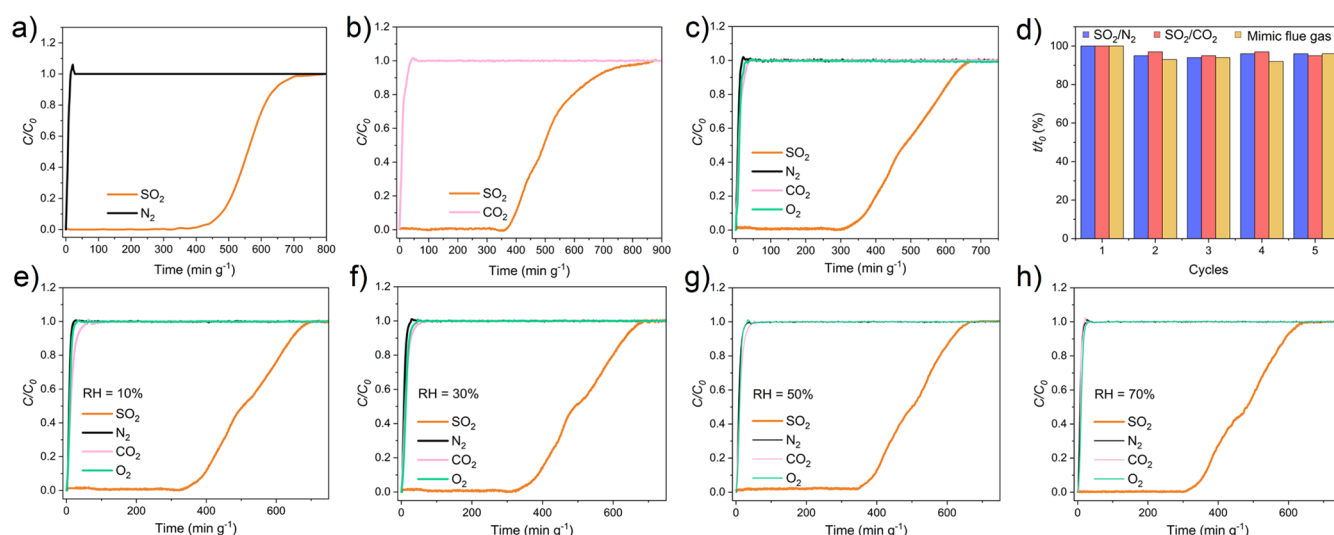


Figure 4. Dynamic separation performance of MMCF-7-AA at 298 K. Experimental column breakthrough curves for: (a) binary SO₂/N₂ mixture (0.25% SO₂, 99.75% N₂); (b) binary SO₂/CO₂ mixture (0.25% SO₂, 99.75% CO₂); and (c) mimic flue gas (0.25% SO₂, 81.63% N₂, 15.1% CO₂, 3.02% O₂). (d) Cycling breakthrough tests for the three gas mixtures (plotted as relative breakthrough time, t/t_0). Breakthrough curves for mimic flue gas under varying relative humidity (RH) conditions: (e) 10% RH, (f) 30% RH, (g) 50% RH, and (h) 70% RH. C/C_0 denotes the ratio of the outlet to inlet concentration.

fitting the single-component gas isotherms collected at 273 and 298 K (Virial method) (Figures S36–S42 and S45–S46). The Q_{st} value of SO₂ (37.73, 45.12, and 50.99 kJ mol⁻¹ for MMCF-5, MMCF-7-AcOH, and MMCF-7-AA, respectively) (Figures 3d and S43) in three MOFs is obviously higher than their corresponding values toward CO₂ (20.52, 21.85, and 26.75 kJ mol⁻¹, Figure S46), indicating that these MOFs have a stronger affinity for SO₂ over CO₂, which is in good correspondence with the previously reported gas-uptake results. It was also observed that the Q_{st} value of SO₂ in MMCF-5, MMCF-7-AcOH, and MMCF-7-AA all tend to gradually decrease with increasing SO₂ loading. According to the Q_{st} curves, when the sites become less available, Q_{st} reduces, but once SO₂ fills the pore, SO₂–SO₂ dipole interactions lead to an increase again in Q_{st} , which is consistent with the results of SO₂ adsorption. Under ideal conditions, the number of captured SO₂ molecules (1 bar) per ligand in MMCF-5, MMCF-7-AcOH, and MMCF-7-AA is calculated to be approximately 12, 13, and 11, respectively (Figure S42). These results also indicate ligand interactions are oversaturated, confirming intermolecular interactions, which is consistent with Q_{st} data. The moderate Q_{st} value of SO₂ assures that MMCF-5/MMCF-7-AcOH/MMCF-7-AA can be regenerated under mild conditions, which offers it great potential for an energy-efficient FGD process.³⁵ To provide a comprehensive benchmarking of SO₂/CO₂ selectivity, we compare MMCF-5, MMCF-7-AcOH, and MMCF-7-AA with representative MOFs at both SO₂/CO₂ = 10/90 and 1/99 compositions (Figure 3f and Table S7), as existing studies report IAST selectivity under different mixture conditions, and neither composition alone captures the full landscape of available data. Based on the available literature data, under SO₂/CO₂ = 10/90, the SO₂/CO₂ selectivity of MMCF-7-AA (Figure S47) is among the highest reported for MOFs to date, exceeded only by Mg-gallate. Under SO₂/CO₂ = 1/99, the SO₂/CO₂ selectivity of MMCF-7-AA again ranks among the highest reported for MOFs, with only Zr-bptc showing a higher value (Table S7).

To evaluate the performance of the actual separation, dynamic breakthrough experiments were conducted using a fixed bed packed with desolvated samples. These experiments were initially conducted using gas mixtures containing 2500 ppm of SO₂ at 298 K and 1.0 bar, balanced with N₂. Consistent with the static sorption tests, MMCF-7-AA exhibits the highest selective retention of SO₂, with a retention time of 390 min g⁻¹, while N₂ elutes rapidly (Figure 4a). MMCF-7-AA also displays the highest dynamic uptakes of SO₂ of 1.30 mmol g⁻¹, while MMCF-5 and MMCF-7-AcOH show dynamic uptakes of 0.30 and 0.68 mmol g⁻¹, respectively (Figures S51 and S52). We further investigated MMCF-7-AA's SO₂ capture capability in the presence of CO₂ (2500 ppm of SO₂ balanced by CO₂), which showed a negligible effect on SO₂ retention. The retention time was 365 min g⁻¹, and the dynamic uptake is 1.24 mmol g⁻¹ (Figure 4b). To further illustrate its outstanding performance in SO₂ removal, breakthrough experiments with mimic flue gas (2500 ppm of SO₂ balanced by 81.63% N₂, 15.1% CO₂, and 3.02% O₂) were conducted for MMCF-7-AA. It continues to demonstrate highly efficient SO₂ removal with a long retention time of 310 min g⁻¹ and a dynamic uptake of 1.15 mmol g⁻¹ (Figure 4c). Recycle tests (Figure 4d) confirm that MMCF-7-AA is robust and show a negligible decrease in dynamic uptake over at least 5 cycles. Besides, considering that under real application conditions there will be moisture effects, we further performed the breakthrough experiments under wet conditions. As illustrated in Figure 4e–h, we introduced water vapor into the mimic flue gas stream with relative humidity (RH) varying from 10% to 70%. Remarkably, MMCF-7-AA exhibited an exceptional tolerance to moisture. The breakthrough profiles remained sharp, with no significant loss in column efficiency. Even under high humidity conditions (70% RH), the material maintained a prolonged retention time of approximately 300 min g⁻¹ (Figure 4h), exhibiting only a minor decrease compared to dry conditions. Consequently, MMCF-7-AA exhibits exceptional selective binding of SO₂ over CO₂, which may have potential applications in cleaning up SO₂ from exhaust gases, where the presence of SO₂ can

poison noble-metal-based catalysts used for selective catalytic reduction.

Investigation of SO₂ Adsorption Mechanism

The observed isotherms for MMCF-7-AcOH and MMCF-7-AA suggest that the SO₂ interaction and clustering mainly occurred at a relatively lower SO₂ pressure. Note that such isotherms for SO₂ sorption have been reported in ultramicroporous materials such as DMOF and M-gallate series, which apparently is not the case for MMCF-7-AcOH and MMCF-7-AA.^{35,36} Inspired by previous reports that identified residual modulator–SO₂ interactions in UIO-66, highlighting the critical role of the modulator in synergistic SO₂ binding, we hypothesize that the *in situ* installed modulator could serve as new binding sites, capable of synergistically interacting with SO₂ alongside the binding sites from the ligand (Figure 6a).¹⁷

In situ diffuse reflectance infrared Fourier transform (DRIFT) measurements were conducted to further investigate the interaction of SO₂ with MMCF-5, MMCF-7-AcOH, and MMCF-7-AA (Figure 5). Given its well-known acidic nature,

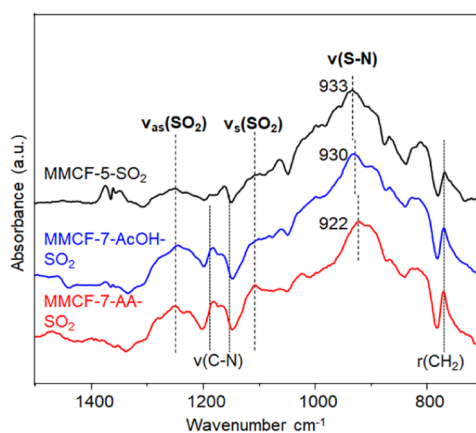


Figure 5. IR difference spectra of SO₂ exposed (at ~75 Torr) MMCF-5 (black), MMCF-7-AcOH (blue), and MMCF-7-AA (red) samples, referenced to the activated samples at room temperature. The SO₂ gas phase was purged away. Notation and acronym: ν , stretching; r , rocking; as , asymmetric; and s , symmetric.

SO₂ is expected to function as a Lewis acid capable of forming charge-transfer complexes with basic sites. This interaction is governed mainly by electrostatic attraction and donor–acceptor interactions involving sulfur-centered antibonding orbitals.^{33,34} After exposure of the samples to SO₂, the difference spectra in Figure 5 show significant SO₂ absorption bands. The bands around 1250 and 1100 cm⁻¹ are attributed to the fundamental stretching modes of adsorbed SO₂ including asymmetric (ν_{as}) and symmetric (ν_s) vibrations.³² Remarkably, both bands exhibit large line width and shifts with respect to the gas phase values at 1362 and 1151 cm⁻¹, indicating they are corresponding to the strongly chemisorbed species.^{32,37} In addition to the $\nu_{as,s}(\text{SO}_2)$ bands, the most striking feature is the intense band around 933–922 cm⁻¹. This is the typical position of $\nu(\text{S–N})$ mode, which appears in various sulfonamides and shows strong intensity.^{38–40} The occurrence of such a mode clearly indicates the formation of N–SO₂ complexes. The positions of $\nu(\text{S–N})$ in MMCF-7-AA and MMCF-7-AcOH are lower than those in MMCF-5. This may be caused by favorable interaction of SO₂ with synergistic binding sites in MOFs through its oxygen site, thus decreasing

the force constant of the S–N bond. Such interactions are directly evidenced by noticeable perturbations occurring to the rocking mode of –CH₂– and stretching modes of C–N (see Figures 2f and 5), as typified by the derivative-like features.^{41,42}

DFT-D calculations were conducted using Gaussian16 to analyze the interactions between SO₂/CO₂ and MMCF-5, MMCF-7-AcOH, and MMCF-7-AA (Figures S54–S60). In three structures, SO₂ forms charge-transfer complexes with the dialkylanilino sites. As shown in Figure 6b, the optimized O₂–

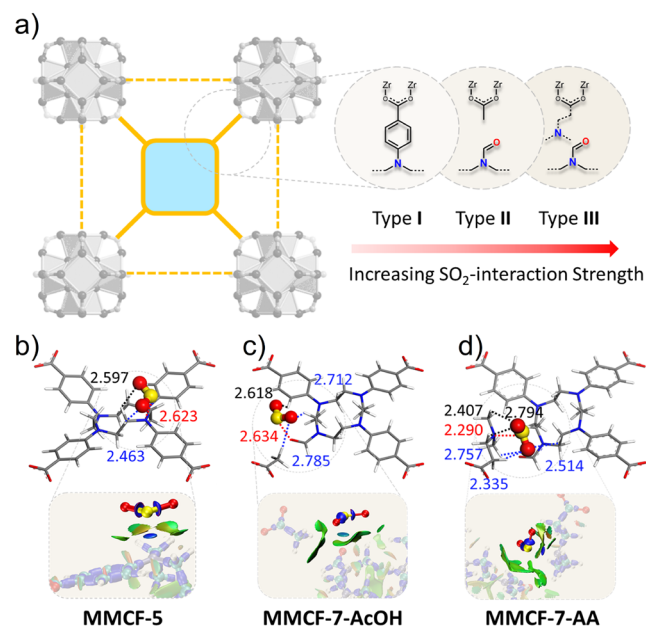


Figure 6. Atomistic-level insights into SO₂ binding. (a) Conceptual representation of the distinct adsorption motifs (Type I, II, and III) engineered within the MMCF series, correlating the structural complexity with increasing interaction strength. Visualization of the dominant binding modes derived from DFT calculations, overlaid with IRI color-filled isosurfaces for (b) MMCF-5, (c) MMCF-7-AcOH, and (d) MMCF-7-AA. The analyses reveal the emergence of multiple cooperative interactions in MMCF-7-AA, verifying the efficacy of the *in situ* generated binding pockets.

S^(δ^+)...(δ^-)N distance was determined to be 2.623 Å. Several C–H^(δ^+)...(δ^-)O=S=O interactions ranging from 2.463 to 2.597 Å were noted as complementary forces. Dialkylanilino was also identified as a major site in MMCF-7-AcOH and MMCF-7-AA (Figures S57 and S59). In addition, SO₂ forms charge-transfer complexes with the *in situ* generated formamide moieties and tertiary amine in MMCF-7-AcOH and MMCF-7-AA. The optimized O₂–S^(δ^+)...(δ^-)O=CH–N distance was determined to be 2.634 Å in MMCF-7-AcOH. Meanwhile, C–H^(δ^+)...(δ^-)O=S=O interactions ranging from 2.618 to 2.785 Å serve as additional stabilizing forces (Figure 6c). In MMCF-7-AA, the optimized O₂–S^(δ^+)...(δ^-)N distance was determined to be 2.290 Å. Additionally, multiple C–H^(δ^+)...(δ^-)O=S=O interactions ranging from 2.335 to 2.794 Å were identified, acting as complementary forces to stabilize the SO₂@MOF adducts (Figure 6d). The calculated binding energies of SO₂ at these *in situ* generated sites within MMCF-7-AcOH and MMCF-7-AA were found to be –52.3 and –61.0 kJ mol⁻¹, respectively, higher than those with MMCF-5 (–42 kJ mol⁻¹) at the dialkylanilino sites, which accounts for enhanced uptake of SO₂ in MMCF-7-AcOH and MMCF-7-AA. Similar to SO₂, the CO₂ molecule is stabilized by electrostatic interactions with

the framework. The binding energies for CO₂ with MMCF-5, MMCF-7-AcOH, and MMCF-7-AA were calculated to be -23.82, -26.35, and -33.15 kJ/mol, respectively. This finding is consistent with and supports the sorption results, where SO₂ exhibited stronger adsorption characteristics. The agreement between the computational and experimental data further validates the selectivity of the MOF toward SO₂ over CO₂.

The electrostatic potential (ESP) and electronic localization function (ELF) maps were calculated to investigate the electron distribution of primary SO₂ binding sites (Figures S61–S63). The ESP mapping at interaction sites displayed distinctive electronic distributions, with electron-rich areas identified at the nitrogen and oxygen sites (colored red) and electron-poor sites on C–H (colored blue). Notably, the *in situ*-formed formamide and dimethyl-propylamine sites in MMCF-7-AA exhibit significantly higher electron cloud density compared to dialkylanilino sites. This stems from the localization of electrons, as their lone pairs are not affected by conjugation effects. The value of ELF analysis at any point ranges between 0 and 1, where ELF = 1/2 corresponds to complete delocalization of electrons similar to a uniform electron gas, whereas ELF = 1 means the perfect localization of an electron in the region. The relatively low ELF value (0.6 to 0.8) between the C and N atoms indicates electron delocalization in the dialkylanilino moieties. In contrast, the formamide and dimethyl-propylamine sites exhibit higher ELF values, reflecting less electron delocalization. In contrast to CO₂, the sulfur atom in SO₂ (a Period 3 element) possesses accessible 3d orbitals and lower-lying antibonding orbitals. This electronic feature allows SO₂ to accept lone pairs more readily, rendering it a significantly more effective Lewis acid. This characteristic makes SO₂ more sensitive to the enhanced Lewis base site, which also matches the microenvironment well to form a stable charge transfer complex.

Additional analysis was performed by using the interaction region indicator (IRI) method. IRI analysis visualizes the formation of noncovalent interactions and serves as a robust tool for investigating the impact of binding geometry.⁴³ The IRI color scale diagram displays three distinct spikes corresponding to ρ indicative of different interactions: attractions (blue spike), van der Waals forces (green), and steric hindrance (red). In Figure 6b–d, all interaction modes are distinctly classified as attractive noncovalent interactions. The visualization of O₂–S^(δ^+)⋯(δ^-)N in MMCF-5/MMCF-7-AA and O₂–S^(δ^+)⋯(δ^-)O in MMCF-7-AcOH displays a deep blue pattern, signifying strong interactions resulting from charge-transfer interactions. C–H^(δ^+)⋯(δ^-)O=S=O is shown in a green color code, indicating attractive interactions stemming from van der Waals forces. The IRI analysis indicates that the interaction between SO₂ and MMCF-5 is relatively weak, partially due to its two-dimensional interaction geometry. In contrast, MMCF-7-AcOH and MMCF-7-AA exhibit stronger interactions with SO₂, which is attributed to the enhanced interaction geometries. Specifically, the binding sites in MMCF-7-AcOH and MMCF-7-AA are more pocket-like, formed by the ligand and the installed modulator. These geometries create a more favorable environment for SO₂ binding, resulting in stronger interactions compared with the planar interacting geometry observed in MMCF-5.

CONCLUSION

In summary, this work introduces ISRE as an approach to overcoming the synthetic limitations of constructing complex

pore environments. By strategically creating a latent reactive handle on a T-shaped ligand (L₂) and triggering its *in situ* editing, we accessed MMCF-7-AA, a material featuring precisely engineered tertiary-amine binding pockets. The resulting framework delivers exceptional SO₂ uptake and selectivity, corroborated by atomistic-level characterizations. Ultimately, these findings highlight the potential of ISRE to bypass the intrinsic trade-off between framework complexity and crystallinity. This strategy provides a versatile pathway to “evolve” simple precursors into high-performance materials, paving the way for porous platforms tailored for other host–guest applications.

ASSOCIATED CONTENT

Supporting Information

The Supporting Information is available free of charge at <https://pubs.acs.org/doi/10.1021/jacs.6c02311>.

Material synthesis; characterization details; supporting figures (PDF)

Accession Codes

Deposition numbers 2395090, 2524745, 2535366, and 2535370 contain the supplementary crystallographic data for this paper. These data can be obtained free of charge via the joint Cambridge Crystallographic Data Centre (CCDC) and Fachinformationszentrum Karlsruhe [Access Structures service](#).

AUTHOR INFORMATION

Corresponding Author

Shengqian Ma – Department of Chemistry, University of North Texas, Denton, Texas 76201, United States;
orcid.org/0000-0002-1897-7069;
Email: Shengqian.Ma@unt.edu

Authors

Junyu Ren – Department of Chemistry, University of North Texas, Denton, Texas 76201, United States
Yanpei Song – Department of Chemistry, University of North Texas, Denton, Texas 76201, United States; orcid.org/0000-0002-4788-5358
Yingxiang Ye – Fujian Provincial Key Laboratory of Polymer Materials, College of Chemistry and Materials Science, Fujian Normal University, Fuzhou, Fujian 350117, China; orcid.org/0000-0003-3962-8463
Peter VanNatta – Department of Chemistry, University of North Texas, Denton, Texas 76201, United States
Yin Zhang – Department of Chemistry, University of North Texas, Denton, Texas 76201, United States; orcid.org/0000-0002-6066-0495
Abdullah M. Al-Enizi – Department of Chemistry, College of Science, King Saud University, Riyadh 11451, Saudi Arabia; orcid.org/0000-0002-3967-5553
Ayman Nafady – Department of Chemistry, College of Science, King Saud University, Riyadh 11451, Saudi Arabia
Kui Tan – Department of Chemistry, University of North Texas, Denton, Texas 76201, United States; orcid.org/0000-0002-5167-7295

Complete contact information is available at: <https://pubs.acs.org/doi/10.1021/jacs.6c02311>

Author Contributions

#J.R. and Y.S. contributed equally.

Notes

The commercial chemicals are used as purchased unless otherwise mentioned. The two ligands were prepared according to procedures described in [Supporting Information](#). The authors declare no competing financial interest.

ACKNOWLEDGMENTS

This work was supported by the Robert A. Welch Foundation (B-0027). Partial support from the Ongoing Research Funding Program (ORF-2026-55), King Saud University, Riyadh, Saudi Arabia (AMA), is also acknowledged.

REFERENCES

- (1) Furukawa, H.; Cordova, K. E.; O’Keeffe, M.; Yaghi, O. M. The chemistry and applications of metal-organic frameworks. *Science* **2013**, *341*, 1230444.
- (2) Zhou, H. C.; Kitagawa, S. Metal-organic frameworks (MOFs). *Chem. Soc. Rev.* **2014**, *43*, 5415–5418.
- (3) Zhou, H. C.; Long, J. R.; Yaghi, O. M. Introduction to metal-organic frameworks. *Chem. Rev.* **2012**, *112*, 673–674.
- (4) Lu, W.; Wei, Z.; Gu, Z. Y.; Liu, T. F.; Park, J.; Park, J.; Tian, J.; Zhang, M.; Zhang, Q.; Gentle, T., III; et al. Tuning the structure and function of metal-organic frameworks via linker design. *Chem. Soc. Rev.* **2014**, *43* (16), 5561–5593.
- (5) Stock, N.; Biswas, S. Synthesis of metal-organic frameworks (MOFs): Routes to various MOF topologies, morphologies, and composites. *Chem. Rev.* **2012**, *112*, 933–969.
- (6) Cohen, S. M. Postsynthetic methods for the functionalization of metal-organic frameworks. *Chem. Rev.* **2012**, *112*, 970–1000.
- (7) Mandal, S.; Natarajan, S.; Mani, P.; Pankajakshan, A. Post-Synthetic Modification of Metal-Organic Frameworks Toward Applications. *Adv. Funct. Mater.* **2020**, *31*, 2006291.
- (8) Bernhardt, P.; Lawrance, G. Complexes of polyaza macrocycles bearing pendent coordinating groups. *Coord. Chem. Rev.* **1990**, *104*, 297–343.
- (9) Liang, X.; Sadler, P. J. Cyclam complexes and their applications in medicine. *Chem. Soc. Rev.* **2004**, *33*, 246–266.
- (10) Yu, X.Y.; Zhang, J. Z. *Macrocyclic polyamines: Synthesis and applications*; Wiley, 2018.
- (11) Shinoda, S. Dynamic cyclen-metal complexes for molecular sensing and chirality signaling. *Chem. Soc. Rev.* **2013**, *42*, 1825–1835.
- (12) Stackhouse, C. A.; Ma, S. Azamacrocyclic-based metal organic frameworks: Design strategies and applications. *Polyhedron* **2018**, *145*, 154–165.
- (13) Gao, W.-Y.; Niu, Y.; Chen, Y.; Wojtas, L.; Cai, J.; Chen, Y.-S.; Ma, S. Porous metal-organic framework based on a macrocyclic tetracarboxylate ligand exhibiting selective CO₂ uptake. *CrystEngComm* **2012**, *14*, 6115–6117.
- (14) Ren, J.; Ye, Y.; Zhang, Y.; Zhang, W.; Liu, Q.; Huang, X.; Al-Enizi, A. M.; Nafady, A.; Liu, J.; Guo, X.; et al. Metal-macrocyclic framework featuring adaptive cavity for precise palladium recognition. *Chemistry* **2024**, *10* (9), 2776–2791.
- (15) Ferrand, A. C.; Imbert, D.; Chauvin, A. S.; Vandevyver, C. D.; Bunzli, J. C. Non-cytotoxic, bifunctional Eu(III) and Tb(III) luminescent macrocyclic complexes for luminescence resonant energy-transfer experiments. *Chemistry* **2007**, *13*, 8678–8687.
- (16) Muzart, J. N. N-Dimethylformamide: much more than a solvent. *Tetrahedron* **2009**, *65*, 8313–8323.
- (17) Walton, I.; Chen, C.; Rimsza, J. M.; Nenoff, T. M.; Walton, K. S. Enhanced Sulfur Dioxide Adsorption in UiO-66 Through Crystal Engineering and Chalcogen Bonding. *Cryst. Growth Des.* **2020**, *20*, 6139–6146.
- (18) Kraus, M. The formylation of aliphatic amines by dimethylformamide. *Synthesis* **1973**, *1973*, 361–362.
- (19) Srivastava, R. K.; Jozewicz, W.; Singer, C. SO₂ scrubbing technologies: A review. *Environ. Prog* **2001**, *20*, 219–228.
- (20) Mathieu, Y.; Tzanis, L.; Soulard, M.; Patarin, J.; Vierling, M.; Molière, M. Adsorption of SO_x by oxide materials: A review. *Fuel Process. Technol.* **2013**, *114*, 81–100.
- (21) Rezaei, F.; Rownaghi, A. A.; Monjezi, S.; Lively, R. P.; Jones, C. W. SO_x/NO_x Removal from Flue Gas Streams by Solid Adsorbents: A Review of Current Challenges and Future Directions. *Energy Fuels* **2015**, *29*, 5467–5486.
- (22) Obeso, J. L.; Flores, C. V.; Peralta, R. A.; Viniegra, M.; Martín-Guaregua, N.; Huxley, M. T.; Solís-Ibarra, D.; Ibarra, I. A.; Janiak, C. Metal-organic frameworks (MOFs) toward SO(2) detection. *Chem. Soc. Rev.* **2025**, *54*, 4135–4163.
- (23) Rieth, A. J.; Wright, A. M.; Dincă, M. Kinetic stability of metal-organic frameworks for corrosive and coordinating gas capture. *Nat. Rev. Mater.* **2019**, *4*, 708–725.
- (24) Islamoglu, T.; Chen, Z.; Wasson, M. C.; Buru, C. T.; Kirlikovali, K. O.; Afrin, U.; Mian, M. R.; Farha, O. K. Metal-Organic Frameworks against Toxic Chemicals. *Chem. Rev.* **2020**, *120*, 8130–8160.
- (25) Ruiz-Castillo, P.; Buchwald, S. L. Applications of Palladium-Catalyzed C-N Cross-Coupling Reactions. *Chem. Rev.* **2016**, *116*, 12564–12649.
- (26) Morris, W.; Voloskiy, B.; Demir, S.; Gandara, F.; McGrier, P. L.; Furukawa, H.; Cascio, D.; Stoddart, J. F.; Yaghi, O. M. Synthesis, structure, and metalation of two new highly porous zirconium metal-organic frameworks. *Inorg. Chem.* **2012**, *51*, 6443–6445.
- (27) Feng, D.; Jiang, H.-L.; Chen, Y.-P.; Gu, Z.-Y.; Wei, Z.; Zhou, H.-C. Metal-Organic Frameworks Based on Previously Unknown Zr₈/Hf₈ Cubic Clusters. *Inorg. Chem.* **2013**, *52*, 12661–12667.
- (28) Huang, N. Y.; Zhang, X. W.; Xu, Y. Z.; Liao, P. Q.; Chen, X. M. A local hydrophobic environment in a metal-organic framework for boosting photocatalytic CO₂ reduction in the presence of water. *Chem. Commun.* **2019**, *55*, 14781–14784.
- (29) Gong, W.; Xie, Y.; Wang, X.; Kirlikovali, K. O.; Idrees, K. B.; Sha, F.; Xie, H.; Liu, Y.; Chen, B.; Cui, Y.; Farha, O. K. Programmed Polarizability Engineering in a Cyclen-Based Cubic Zr(IV) Metal-Organic Framework to Boost Xe/Kr Separation. *J. Am. Chem. Soc.* **2023**, *145*, 2679–2689.
- (30) Düren, T.; Millange, F.; Férey, G.; Walton, K.S.; Snurr, R.Q. Calculating Geometric Surface Areas as a Characterization Tool for Metal-Organic Frameworks. *J. Phys. Chem. C* **2007**, *111*, 15350–15356.
- (31) First, E. L.; Gounaris, C. E.; Wei, J.; Floudas, C. A. Computational characterization of zeolite porous networks: An automated approach. *Phys. Chem. Chem. Phys.* **2011**, *13*, 17339–17358.
- (32) Hadjiivanov, K. I.; Panayotov, D. A.; Mihaylov, M. Y.; Ivanova, E. Z.; Chakarova, K. K.; Andonova, S. M.; Drenchev, N. L. Power of Infrared and Raman Spectroscopies to Characterize Metal-Organic Frameworks and Investigate Their Interaction with Guest Molecules. *Chem. Rev.* **2021**, *121*, 1286–1424.
- (33) Li, J.; Rogachev, A. Y. SO₂-yet another two-faced ligand. *Phys. Chem. Chem. Phys.* **2015**, *17*, 1987–2000.
- (34) Oh, J. J.; La Barge, M. S.; Matos, J.; Kampf, J. W., II; Hillig, K. W.; Kuczkowski, R. L. Structure of the Trimethylamine-Sulfur Dioxide Complex. *J. Am. Chem. Soc.* **1991**, *113*, 4732–4738.
- (35) Chen, F.; Lai, D.; Guo, L.; Wang, J.; Zhang, P.; Wu, K.; Zhang, Z.; Yang, Q.; Yang, Y.; Chen, B.; Ren, Q.; Bao, Z. Deep Desulfurization with Record SO₂ Adsorption on the Metal-Organic Frameworks. *J. Am. Chem. Soc.* **2021**, *143*, 9040–9047.
- (36) Xing, S.; Liang, J.; Brandt, P.; Schäfer, F.; Nuhnen, A.; Heinen, T.; Boldog, I.; Möllmer, J.; Lange, M.; Weingart, O.; et al. Capture and Separation of SO₂ Traces in Metal-Organic Frameworks via Pre-Synthetic Pore Environment Tailoring by Methyl Groups. *Angew. Chem., Int. Ed.* **2021**, *60* (33), 17998–18005.
- (37) Tobin, R. G. Vibrational Linewidths of Adsorbed Molecules: Experimental Considerations and Results. *Surf. Sci.* **1987**, *183*, 226–250.
- (38) Gowda, B. T.; Jyothi, K.; D’Souza, J. D. Infrared and NMR spectra of arylsulphonamides, 4-X-C₆H₄SO₂NH₂ and iX, j-

$YC_6H_3SO_2NH_2$ ($x = H; CH_3; C_2H_5; f; Cl; Br; I$ or NO_2 and $iX, jY = 2, 3-(CH_3)_2; 2, 4-(CH_3)_2; 2, 5-(CH_3)_2; 2-CH_3, 4-Cl; 2-CH_3, 5-Cl; 3-CH_3, 4-Cl; 2, 4-Cl_2$ or $3, 4-Cl_2$). *Z. Naturforsch., A* **2002**, *57*, 967–973.

(39) Uno, T.; Machida, K.; Hanai, K.; Sasaki, S.; Ueda, M.; Sasaki, S. Infrared Spectra of Sulfonamide Derivatives. I. Pyridine, Thiazole, and Pyrimidine Derivatives. *Chem. Pharm. Bull.* **1963**, *11* (6), 704–708.

(40) Misaela, F.-M.; Alexander, P. D. L. L.; Catalina, S.-C.; Carolina, B.-S.; Ignacio, S.-D. C. Tautomerism and IR spectroscopy of arylsulfonamides by quantum mechanical calculations. *J. Mol. Struct.* **2022**, *1250*, 131717.

(41) Li, H.-W.; Strauss, H. L.; Snyder, R. G. Differences in the IR Methylene Rocking Bands between the Crystalline Fatty Acids and n-Alkanes: Frequencies, Intensities, and Correlation Splitting. *J. Phys. Chem. A* **2004**, *108*, 6629–6642.

(42) Smith, B. C. Organic Nitrogen Compounds V: Amine Salts. *Spectrosc* **2019**, *34*, 30–37.

(43) Lu, T.; Chen, Q. Interaction Region Indicator: A Simple Real Space Function Clearly Revealing Both Chemical Bonds and Weak Interactions. *Chem. Methods* **2021**, *1*, 231–239.



CAS INSIGHTS™

EXPLORE THE INNOVATIONS SHAPING TOMORROW

Discover the latest scientific research and trends with CAS Insights. Subscribe for email updates on new articles, reports, and webinars at the intersection of science and innovation.

Subscribe today

CAS
A Division of the
American Chemical Society